Hydrodynamics simulations of 2 (omega) laser propagation in underdense gasbag plasmas

N. B. Meezan, L. Divol, M. M. Marinak, G. D. Kerbel, L. J. Suter, R. M. Stevenson, G. E. Slark, K. Oades

April 27, 2004

Physics of Plasmas

Disclaimer

Hydrodynamics simulations of 2ω laser propagation in underdense gasbag plasmas.

N. B. Meezan,* L. Divol, M. M. Marinak, G. D. Kerbel, and L. J. Suter

Lawrence Livermore National Laboratory,

P.O. Box 808, Livermore, CA, 94551-0808

R. M. Stevenson, G. E. Slark, and K. Oades

Atomic Weapons Establishment, plc., Aldermaston, Berkshire, U.K.

Abstract

Recent 2ω laser propagation and stimulated Raman backscatter (SRS) experiments performed on the Helen laser have been analyzed using the radiation-hydrodynamics code HYDRA. These experiments utilized two diagnostics sensitive to the hydrodynamics of gasbag targets: a fast x-ray framing camera (FXI) and an SRS streak spectrometer. With a newly implemented nonlocal thermal transport model, HYDRA is able to reproduce many features seen in the FXI images and the SRS streak spectra. Experimental and simulated side-on FXI images suggest that propagation can be explained by classical laser absorption and the resulting hydrodynamics. Synthetic SRS spectra generated from the HYDRA results reproduce the details of the experimental SRS streak spectra. Most features in the synthetic spectra can be explained solely by axial density and temperature gradients. The total SRS backscatter increases with initial gasbag fill density up to ≈ 0.08 times the critical density, then decreases. Images from a near-backscatter camera (NBI) show that severe beam spray is not responsible for the trend in total backscatter. Filamentation does not appear to be a significant factor in gasbag hydrodynamics. The simulation and analysis techniques established here can be used in upcoming experimental campaigns on the Omega laser facility and the National Ignition Facility.

PACS numbers: Valid PACS appear here

---

*Electronic address: `meezan1@llnl.gov`

I.   INTRODUCTION

The prospect of operating the National Ignition Facility (NIF) at 2ω offers several potential advantages to reaching ignition. Capsule designs that take advantage of high absorbed power and large fuel mass can obtain robust, high-yield burns. Unfortunately, high $I\lambda^2$ and long length-scales can lead to destructive parametric instabilities. Filamentation and stimulated Raman (SRS) and Brillouin (SBS) backscatter can degrade hohlraum conversion efficiency and symmetry. Hot electrons generated by SRS saturation can catastrophically pre-heat the capsule fuel [1]. Surmounting these problems requires a solid understanding of 2ω laser propagation and backscatter in long, underdense plasmas.

II.   GASBAG EXPERIMENTS AT HELEN

Experiments have been conducted at AWE's Helen laser [2] to investigate 2ω propagation and interaction physics [3] . Gasbag targets were used to approximate the long, underdense plasma that would occur in a NIF 2ω ignition hohlraum. An LLNL gasbag consists of an aluminum washer of inner diameter 2.8 mm with a thin polyimide ($C_{22}H_{10}N_2O_4$) skin bonded to each end. When inflated, a gasbag forms an oblate ellipsoid ≈ 2.4 mm long, with a skin thickness of 0.35-0.4 µm [4]. The gasbags were filled with neopentane (C_5H_{12}) to obtain SRS-producing plasmas with electron densities 4% to 26% of the critical density.

A schematic of the experimental setup is shown in Fig. 1. One arm of the Helen laser was used to generate a 1 ns approximately square pulse with 300-400 J of energy. The shots
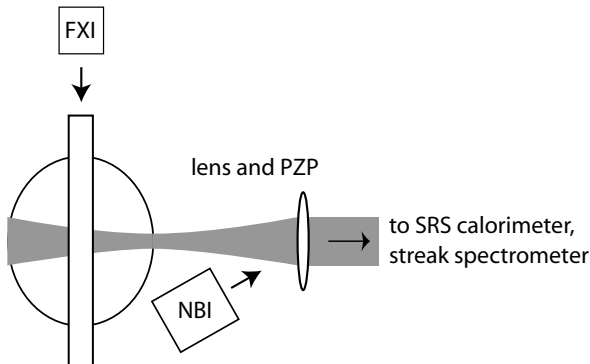

FIG. 1: Schematic of Helen gasbag experiments.

described here used a phase zone plate (PZP) [5] to focus the beam to a smooth, flat (4th-order super-Gaussian) 250 µm diameter spot on the surface of the front skin, corresponding to an intensity $I \leq 8 \times 10^{14}$ W/cm^2. The optical train had an overall f-number of about 3. Unlike previous gasbag experiments performed at multi-beam facilities, these experiments do not examine an interaction beam propagating through a pre-formed plasma [6]. Laser propagation and interaction occur simultaneously.

A side-on fast x-ray imaging camera (FXI) imaged the bags to observe laser propagation and hydrodynamics. A 25 µm thick beryllium filter shielded photons below 1 keV. The FXI took 100 ps snapshots of the gasbag at times $t \approx 0$ ns, 0.36 ns, 0.86 ns, and 1.25 ns, where $t = 0$ indicates the start of the laser pulse. The snapshots were approximately 100 ps long, with a timing uncertainty of about 150 ps. A small amount (1 % by partial pressure) of krypton was added to some bags to enhance the x-ray images. The SRS station collected light scattered back into the main focusing optics. A calorimeter measured total (time-integrated) backscatter, while a streak camera and grating spectrometer recorded time-resolved spectra. To give a qualitative estimate of the SRS scattered outside the collection optics, a filtered near-backscatter imaging (NBI) camera was focused on a diffuse aluminum plate surrounding the beam entrance window. A similar set-up was used to measure SBS. The SBS measured for the neopentane gasbags was generally less than 2% of the input laser energy. For the shots described in this paper, the SBS fraction was below 1%.

III. SIMULATIONS AND MODELING

A. Hydrodynamics simulations

Radiation-hydrodynamics simulations of the gasbags were performed in HYDRA to assist in the analysis of the experiments. HYDRA is a 2D/3D multi-physics code based originally on a hydrodynamics package by R. Tipton and developed by M. M. Marinak for inertial confinement fusion simulations [7]. In the experiment, the beam is incident along the axis of symmetry, so the gasbags were modeled in 2-D as 2.4 mm diameter spheres. HYDRA's laser ray-tracing package includes inverse bremsstrahlung absorption, bulk refraction, ponderomotive effects, and turning-point energy deposition, but did not capture speckle-scale laser-plasma physics in these simulations. The laser beam power was taken from the actual

experimental shot for each simulation, with 600 laser rays per beam.

The simulations also included multigroup radiation diffusion with tabular opacities calculated assuming local thermodynamic equilibrium (LTE). Radiation transport is not very important in these low-Z plasmas. The hydrodynamics for these simulations were fully Lagrangian. An analytical equation of state (QEOS) [8] with separate electron and ion temperatures was used for all materials. The aluminum washer was not modeled.

B.   Electron thermal conduction

Recently, a kernel-based nonlocal electron thermal conduction package based on the model developed by Shurtz *et al.*[9] was installed in HYDRA [10]. Previously, HYDRA modeled only gradient-driven (local) electron thermal conduction with a hard flux limit. For the local model, the maximum heat flux allowed across a given surface is some fraction f (the flux limiter) of the "free-streaming" heat flux,

$$q = \min(-\kappa \nabla T_e, f \times q_{fs}),$$

where

$$q_{fs} = (n_e k_B T_e) \, v_{te}.$$

Here, n_e is the electron density, T_e is the electron temperature, k_B is Boltzmann's constant and $v_{te} = \sqrt{k_B T_e / m_e}$ is the electron thermal velocity.

The nonlocal model, which does not require the adjustable parameter f, handles the effects of long-range electrons, for which the energy-transfer mean free path is long compared to the temperature gradient length scale. Depending on the properties of the plasma, the nonlocal heat flux into a particular zone can be greater than or less than the calculated local heat flux $q = -\kappa \nabla T_e$. The importance of accurately calculating the heat transport in the gasbag will be discussed later in the paper.

C.   Synthetic FXI images

The results of each HYDRA simulation were post-processed to generate synthetic x-ray images for corroboration with the FXI images. An array of straight rays, each corresponding to an FXI pixel, was traced through the HYDRA mesh. The radiation transport equation was

then integrated along each ray, using the resultant n_e, T_e, and LTE opacities. The result was convolved with the filter function of the 25 µm Be filter to remove x-rays below ≈ 1 keV. To account for the 100 ps resolution of the FXI camera, 10 ray-tracings performed at 10 ps intervals were summed to produce each image.

Emission from the polyimide skin was much brighter in the synthetic images than in the experimental images. We believe this is an artifact due to the LTE opacities used in the simulations, so the skin emission was removed from the synthetic images. The grayscales of the synthetic images were adjusted to qualitatively match the experimental images. The bottom of the grayscale (white) was placed below zero to mock-up the background seen in the experiments. Similarly, the top (black) of the grayscale was placed below the peak intensity to mock-up saturation. The grayscales remained linear with energy.

D.   Synthetic SRS spectra

The simulation results were also post-processed for comparison to the time-resolved SRS spectra. At 10 ps intervals, 6 rays evenly spaced in radius were traced along the laser axis. The simulated electron density n_e and T_e were interpolated onto the ray paths, then averaged over the six rays. The resulting smooth profiles were input into NEWLIP, a package developed by E. A. Williams for performing linear laser-plasma interaction calculations [11]. The laser intensity was estimated from the input intensity by accounting for inverse bremsstrahlung absorption and defocusing. This agreed well with the zonal laser intensity output by HY-DRA, but was spatially less noisy. At each time, the local SRS spatial gain coefficient was calculated and integrated along the ray path as a function of scattered wavelength, giving the time-resolved spectrum of the gain coefficient. Once the gain spectrum is smoothed to match the resolution of the experimental device, it can be qualitatively compared to the experimental streak spectrum.

IV.   RESULTS AND ANALYSIS

A.   Laser propagation and hydrodynamics

Interpreting the Helen experiments requires understanding the macroscopic hydrodynamics of gasbags. The axial electron density and electron temperature profiles from one

simulation are shown for three different times in Fig. 2. The laser beam rapidly deposits energy into the bag skin, causing it to ionize and explode. When the skin plasma falls below the critical density, the beam begins to propagate across the bag as a supersonic "bleaching" (ionization) wave, creating a long interaction plateau. The rapid heating of the laser channel drives a subsonic heat front radially outward. The plasma expands behind the wave, decreasing the electron density of the plateau. Simultaneously, blast waves form at the front and (later) back sides of the bag. The two blast waves propagate towards the center of the bag, shrinking the plateau.
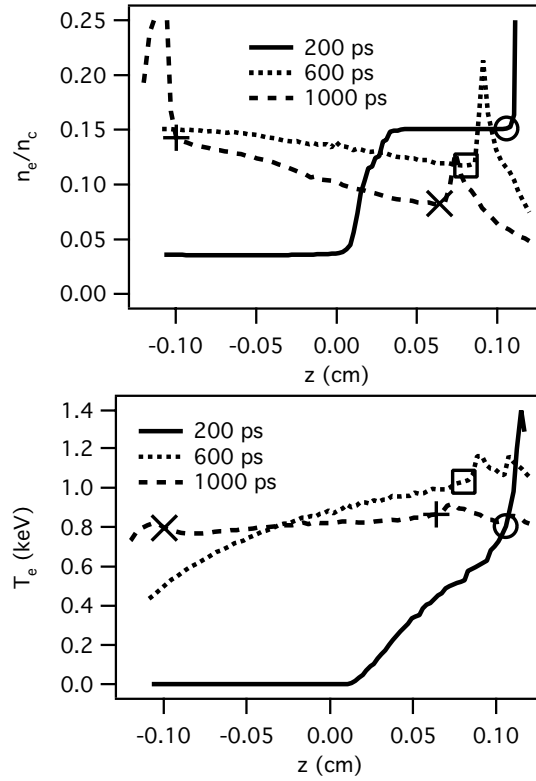

FIG. 2: Lineouts of simulated electron density (top) and electron temperature (bottom) at three times for Helen shot 2305 (initial fill density $n_e = 0.15\,n_c$).

The rate at which the bleaching and radial expansion occur depends on the interplay between heating of the laser channel by inverse bremsstrahlung and cooling by electron thermal conduction. If heat flows rapidly into the surrounding cold gas, the bleaching wave propagates slowly across the bag. The heat front will drive a weak cylindrical density wave that propagates radially outward at a speed comparable to that of the bleaching wave. If the lateral heat flow is slow, the channel will heat rapidly. The bleaching wave will propagate

6

TABLE I: Electron temperature range for the experiments

$n_e/\,n_c$	0.05	0.10	0.15
T_e (eV)	500 to 600	600 to 800	400 to 1000

quickly across the bag, while the slow radial density wave follows the laser beam closely. The dynamic behavior of the gasbags makes it difficult to give one characteristic temperature for each experiment. Table I shows the approximate temperature range of the plateau.

The behavior of the thermally-driven waves in the gasbag shows up clearly in the synthetic FXI images. In general, the high density regions of the plasma dominate the emission. The extents of the FXI images are determined by the axial blast waves moving in from the front and back of the bag and by the radial wave driven by the laser channel. Figure 3 compares the experimental image for shot 1811, a gasbag with initial fill density $n_e = 0.16\ n_c$, to synthetic FXI images from simulations with three different thermal conductivity models. Shot 1811 was chosen for Fig. 3 because it best illustrates how the choice of thermal transport model affects the simulated FXI images.

The simulation using local transport with a "traditional" flux limiter of $f = 0.05$ (Fig. 3b.) shows the poorest agreement with the experimental images. The radial heat flow from the laser-heated channel is restricted, so the laser forms a hot channel in the plasma and propagates through the plasma too quickly. The cylindrical wave generated by the laser channel follows the shape of the f/3 beam, expanding from right to left. In addition, the time required for the laser to propagate across the bag is clearly too short. A local simulation with $f = 1$ (Fig. 3c.) better reproduces the experimental images and the rate of laser propagation. Heat flows out radially faster than the channel forms axially, resulting in an image that narrows from right to left. The nonlocal simulation (Fig. 3d.) also resembles the experimental data, although it does slightly over-predict the propagation speed of the channel.

Figure 4 shows synthetic and experimental FXI images for a scaling of initial gasbag fill density ($n_e/n_c = 0.08$, 0.12, and 0.16 times n_c). The synthetic images were generated from simulations using the nonlocal heat transport model. In general, agreement between the experimental and simulated images was quite good. For example, the degree of propagation and propagation times for the simulated images are very close to the experimental images.
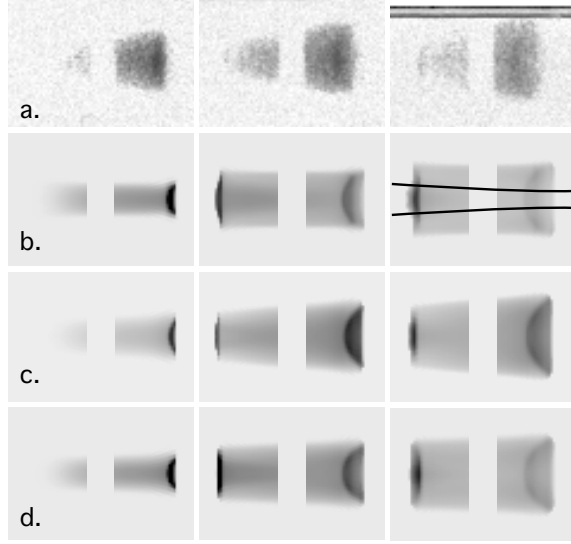
FIG. 3: Experimental and synthetic FXI images for shot 1811 ($n_e = 0.16$ n_c), at (left) 360 ps, (middle) 860 ps, and (right) 1250 ps from the start of the laser pulse. The laser travels from right to left. (a). Experiment, (b.) Local conduction, $f = 0.05$, (c.) Local conduction, $f = 1.0$, (d.) Nonlocal conduction. The rays drawn onto the third frame of (b.) show the extent of the f/3 beam.

This suggests that our simulations of the gasbag hydrodynamics are mostly correct. On the other hand, the simulated images tend to have less right-to-left taper than the experimental images. The simulated image for the $n_e = 0.08$ n_c case actually has a slight right-to-left taper. Analysis is underway to resolve this discrepancy. It is possible that using a non-LTE model for the opacities (not available for these simulations) could effect the results.

The synthetic images are generally slightly (.1 to .2 mm) longer than the experimental images. The gasbag radius used in the simulations shown here corresponds to a bag filled with 1 bar of gas at room temperature; however, most of the gasbags were filled to less than 1 bar to get the desired electron density. Pre-shot pictures of the targets are not available, so the exact initial radius of each target is not known (the aluminum washer in the x-ray images is the only spatial reference).

Grid and timestep convergence studies have been performed to see the spatial or temporal resolution of the simulations are sufficient to capture the physics of the experiments. HYDRA has automatic timestep control and uses the most restrictive of several criterea to choose the next timestep. For these simulations, the timestep tended to be limited by the change
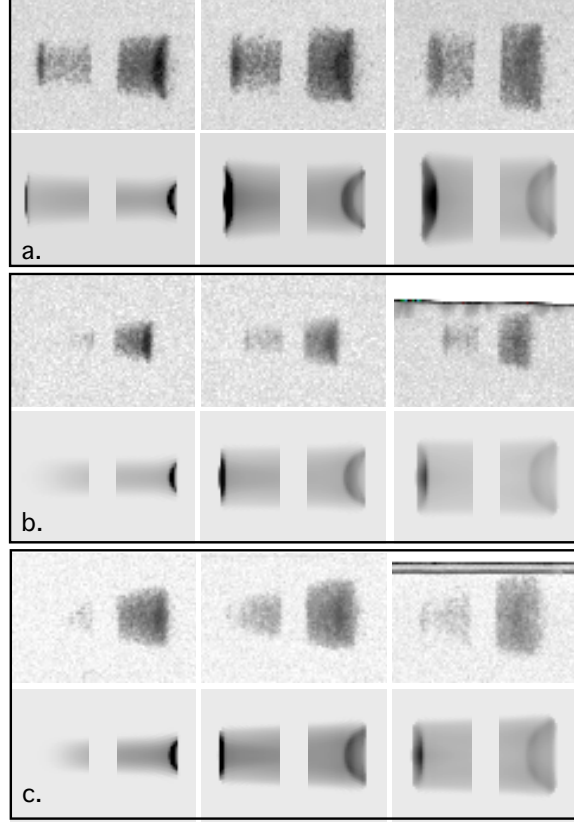
FIG. 4: Experimental and synthetic FXI images for shots (a.) 1825 ($n_e = 0.08$ n_c), (b.) 1813 ($n_e = 0.12$ n_c), and (c.) 1811 ($n_e = 0.16$ n_c). Frame times are as in Fig. 3. The top row of each group is the experimental image.

in electron temperature due to laser absorption and electron thermal conduction. We ran simulations with a smaller average timestep by decreasing the maximum allowed fractional temperature change per cycle. Decreasing the timestep by a factor of 3-9 results in slightly different evolution of the blast waves in the gasbag. However, the qualitative results, i.e., the synthetic x-ray images, are not significantly changed. Similarly, increasing the number of zones in the problem by a factor of 2-4.5 results in smoother reproduction of the front blast wave but does not significantly change the synthetic images.

B. Raman streak spectra

The total SRS backscatter for each shot is plotted against initial electron density in Fig. 5. As the initial density in the pure pentane bags increases, the SRS increases, peaking at 30 % near $n_e = 0.08\ n_c$. As density increases further, the total backscatter drops. The increase in backscatter with density is easily explained, as the SRS gain coefficient increases with density. The subsequent decrease beyond $0.1\ n_c$ is more difficult to understand. Damping and kinetic effects are not expected to play a strong role in these plasmas, as $k\lambda_{De} \approx 0.1$ to 0.3. The damping rate decreases with increasing initial density, which would not explain the drop in backscatter with increasing density.
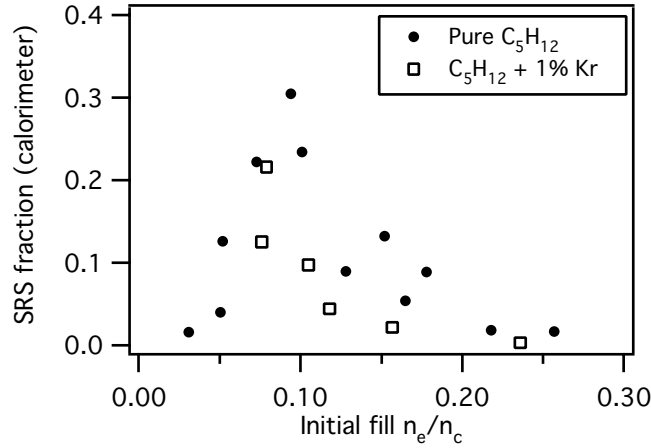

FIG. 5: Total SRS backscatter (fraction of input laser energy) as a function of initial gasbag fill density. Kr-doped bags have lower total SRS, but show the same trend with initial fill density.

One possible explanation is that the beam strongly filaments for $n_e \geq 0.08\ n_c$. The subsequent backscatter would then spread beyond the f/3 collection cone of the optics, resulting in an artificial drop in calorimeter signal. This hypothesis is seemingly supported by the SRS streak spectra, shown in the top row of Fig. 6. The broadening of the spectra with initial gasbag fill density appears to reveal the onset of filamentation above $n_e \approx 0.08\ n_c$. However, the simulated SRS spectra generated by post-processing the HYDRA results (with nonlocal thermal transport), shown in the bottom row of Fig. 6, show that the spread of the SRS spectra with increasing fill density can be explained solely by bulk hydrodynamics. At low density ($< 0.1\ n_c$), the synthetic spectra are both straight and narrow. As density
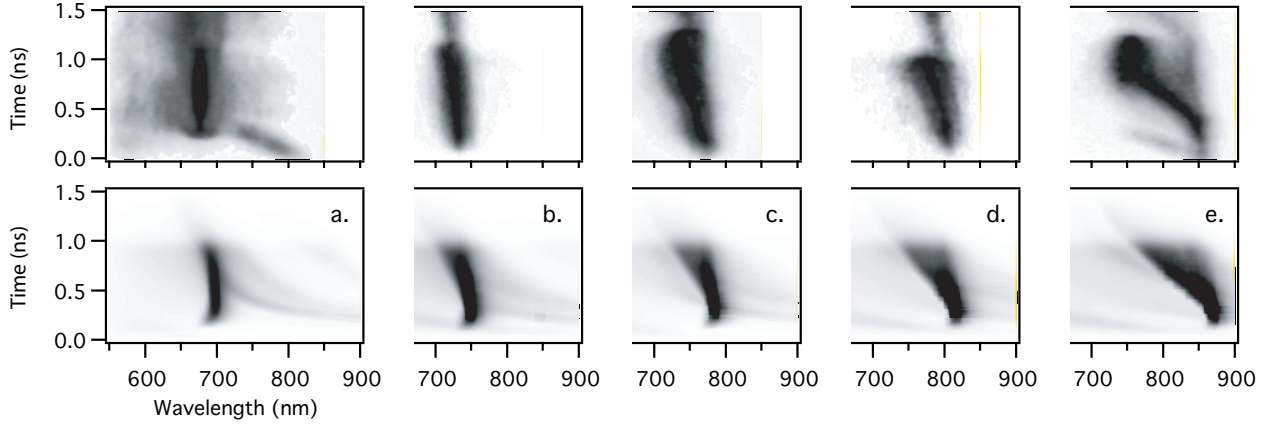
10

FIG. 6: Experimental (top) and synthetic SRS streak spectra. (a.) Shot 2303, 0.05 n_c. (b.) Shot 1809, 0.08 n_c. (c.) Shot 2304, 0.1 n_c. (d.) Shot 1813, 0.12 n_c. (e.) Shot 2305, 0.15 n_c. The synthetic streak spectra have been smoothed in wavelength and time using a boxcar filter to match the resolution of the spectrometer. For the synthetic spectra, the grayscales are limited to a gain of 5-7 to mock up saturation and allow qualitative comparison to the experimental data.

increases, the spectra broaden and tilt towards the laser wavelength of 527 nm, in close agreement with the experimental spectra.

The role of hydrodynamics forming the SRS spectra is more clearly seen by comparing Figs. 2 and 7(d.). The three markers on Fig. 2 identify (n_e, T_e) pairs that correspond to the times and backscattered wavelengths on the synthetic spectrum for Fig. 7(d.). At early time, the bleaching wave is only halfway across the channel. The density plateau is short and flat, so the gain spectrum is narrow. At late time, the right side of the channel has expanded to low density, corresponding to a wavelength closer to the laser wavelength. The low-wavelength (left) side of the SRS streak spectrum shows light scattered from the front of the gasbag, immediately behind the axial bast wave. The high-wavelength (right) side of the spectrum shows light from the far side of the gasbag. Axial gradients can explain the tilt and spread of the spectrum almost entirely. The NBI images, shown in Fig. 8 further suggest that filamentation plays a minor role in explaining the trend seen in the total backscatter data. The low signal at higher density is consistent with lower total backscatter, not with backscatter outside of the beam cone.

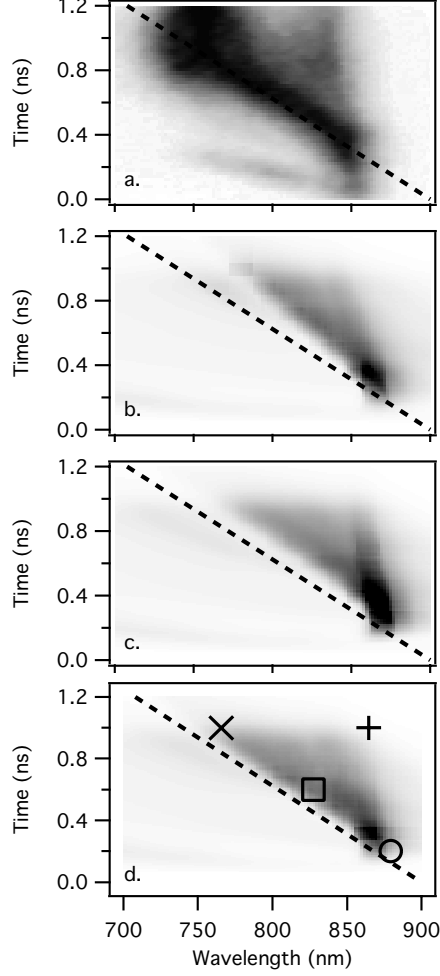The SRS spectra are also useful for comparing thermal conduction models. Figure 7

11

FIG. 7: Comparison of simulated SRS spectra for shot 2305 (0.15 n_c) for different thermal transport models. (a.) Experiment (b.) Flux-limited, $f = 1.0$ (c.) Flux-limited, $f = 0.05$ (d.) Nonlocal. The markers in (d.) correspond to Fig. 2. The grayscale limit has been increased to 10 to allow the markers to be visible.

shows SRS spectra for shot 2305 (0.15 n_c) for three different thermal transport models. This slope of the SRS wavelength with time (shown by the dotted line) indicates the rate at which the central channel expands and should be reproduced in hydrodynamics simulations. The simulation using local transport with $f = 0.05$ does a good job of reproducing the slope; however, as shown in Fig. 3, this model is poor with regard to the FXI propagation images. The $f = 1$ simulation agreed reasonably well with the FXI data and qualitatively matches the SRS data, but the slope of the simulated spectrum is too shallow. The nonlocal simulation, which also agreed reasonably well with the FXI data, is able to reproduce the slope of
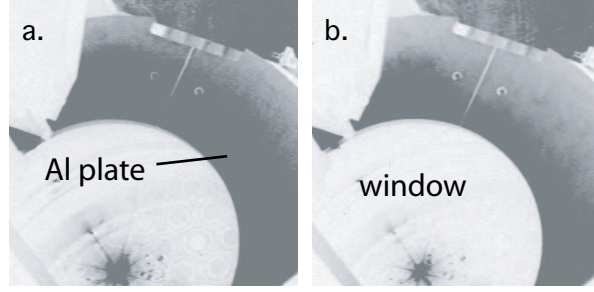
FIG. 8: Near-backscatter images from shots (a.) 2304 (initial $n_e = 0.10 \ n_c$) and (b.) 2305 (initial $n_e = 0.15 \ n_c$). Dark indicates higher signal.

the SRS spectrum. Compared to an $f = 1$ local simulation, the nonlocal model results in decreased heat flux at steep temperature gradients. Unlike a severely flux-limited ($f = 0.05$) simulation, the nonlocal model allows faster electrons to preheat the cold gas ahead of the main temperature wave. The nonlocal simulation results in physically reasonable axial and radial density gradients and qualitatively recreate both experimental diagnostics. The timestep and grid convergence studies described in section IV A did not change the qualitative behavior of the SRS streak spectra.

C. Total Raman backscatter

Axial density gradients may also help explain the drop in total SRS seen at high density in Fig. 5. Lower density bags absorb less strongly and have weaker radial thermal waves, so the plateaus remain flat. At higher density, axial density gradients result in shorter resonant lengths along which SRS waves can grow. The higher absorption also results in lower intensity along the channel, further lowering the SRS gain. The peak gain calculated from simulations roughly follows the trend in Fig. 5, increasing until $n_e = 0.12 n_c$ and then decreasing. Nonetheless, it is difficult to use the SRS gain spectra calculated from NEWLIP to make a definitive, quantitative argument that hydrodynamics alone can explain the trends seen in Fig. 5. Additional physical effects, such as electron plasma wave saturation, must be included to definitively explain Fig. 5. The peak post-processed gains are all well above 20, a value at which one might expect wave saturation. The total SRS detected in the experiment is reabsorbed in the axial blast wave driven from the front of the gasbag and is therefore

13

sensitive to the peak density of that wave. The hydrodynamics simulations described here are a necessary first step towards fully explaining the total detected Raman backscatter in this and other experiments.

V. CONCLUSIONS

Radiation-hydrodynamics simulations in HYDRA have been applied to the analysis of 2ω laser propagation and Raman backscatter experiments performed on the Helen laser. Experimental and simulated FXI images imply that the beam propagates across the gasbags in a straightforward way: Propagation can be explained by classical laser absorption and the resulting hydrodynamics, without invoking filamentation. NBI images also rule out severe beam spray. Synthetic SRS spectra accurately reproduce the tilt and spread of the experimental SRS streak spectra. The nonlocal thermal transport model is best able to reproduce both the FXI images and the SRS streak spectra. The streak spectra also seem to be explained by straightforward gasbag hydrodynamics, as most features of the spectra can be explained solely by axial density and temperature gradients. Axial gradients may also explain the trend in total SRS with gasbag density; however, further analysis is needed. The simulation and analysis tools developed here will aid in the interpretation of future laser-plasma interaction experiments.

---

[1] J. D. Lindl, *Inertial Confinement Fusion* (Springer, 1998).

[2] M. J. Norman, J. E. Andrew, T. H. Bett, R. K. Clifford, J. E. England, N. W. Hopps, K. W. Parker, K. Porter, and R. M. Stevenson, Appl. Optics **41**, 3497 (2002).

[3] R. M. Stevenson, L. J. Suter, K. Oades, W. Kruer, G. E. Slark, K. Fournier, N. Meezan, R. L. Kauffman, M. Miller, S. Glenzer, et al., Phys. Plasmas (2004), accepted for publication.

[4] R. Wallace, personal communication.

[5] T. H. Bett, C. N. Danson, P. Jinks, D. A. Pepler, I. N. Ross, and R. M. Stevenson, Appl. Opt. **34**, 4025 (1995).

[6] J. D. Moody, B. J. Macgowan, R. L. Berger, K. G. Estabrook, S. H. Glenzer, R. K. Kirkwood, W. L. Kruer, G. E. Stone, and D. S. Montgomery, Phys. Plasmas **7**, 3388 (2000), and references therein.

[7] M. M. Marinak, G. D. Kerbel, N. A. Gentile, O. Jones, D. Munro, S. Pollaine, T. R. Dittrich, and S. W. Haan, Phys. Plasmas **8**, 2275 (2001).

[8] R. M. More, K. H. Warren, D. A. Young, and G. B. Zimmerman, Phys. Fluids **31**, 3059 (1988).

[9] G. P. Shurtz, P. D. Nicolaï, and M. Busquet, Phys. Plasmas **7**, 4328 (2000).

[10] G. D. Kerbel, unpublished (2003).

[11] E. A. Williams, Lawrence Livermore National Laboratory ICF Annual Report (UCRL-LR-105820-98) p. 13 (1998).